PHYSICAL REVIEW B **110**, 054207 (2024)

Disorder free many-body localization transition in two quasiperiodically coupled Heisenberg spin chains

K. G. S. H. Gunawardana[1] and Bruno Uchoa[2,*]
[1]*Department of Engineering Technology, Faculty of Technology, University of Ruhuna, Matara 81000, Sri Lanka*
[2]*Department of Physics and Astronomy, University of Oklahoma, Norman, Oklahoma 73069, USA*

(Received 11 May 2024; accepted 12 August 2024; published 28 August 2024)

Disorder free many-body localization (MBL) can occur in interacting systems that can dynamically generate their own disorder. We address the thermal-MBL phase transition of two isotropic Heisenberg spin chains that are quasiperiodically coupled to each other. The spin chains are incommensurate and are coupled through a short-range exchange interaction of the XXZ type that decays exponentially with the distance. Using exact diagonalization, matrix product states, and a density matrix renormalization group, we calculate the time evolution of the entanglement entropy at long times and extract the inverse participation ratio in the thermodynamic limit. We show that this system has a robust MBL phase. We establish the phase diagram with the onset of MBL as a function of the interchain exchange coupling and of the incommensuration between the spin chains. The Ising limit of the interchain interaction optimizes the stability of the MBL phase over a broad range of incommensurations above a given critical exchange coupling. Incorporation of interchain spin flips significantly enhances entanglement between the spin chains and produces delocalization, favoring a prethermal phase whose entanglement entropy grows logarithmically with time.

DOI: 10.1103/PhysRevB.110.054207

I. INTRODUCTION

Many-body localization (MBL) describes a dynamical phase of an interacting quantum system that cannot reach thermal equilibrium in the thermodynamic limit [1–10]. The growth of entanglement with time within an isolated system is inhibited in the MBL phase, resulting in nonergodic time evolution and area law scaling of the entanglement entropy. A thermal phase in contrast follows ergordic time evolution, developing full entanglement in the Hilbert space and volume law scaling of entanglement entropy. Thus, a hallmark of the MBL phase is the onset of very slow dynamics that preserves information of the initial quantum state [11–15]. MBL states have been experimentally observed in optical lattices with cold atoms systems [15,16], where the entanglement entropy can be directly measured [17], and also in circuits with superconducting qubits [18,19]. Those states are of technological importance in the development of quantum memory [20–23] and also of fundamental interest to subjects ranging from quantum information, time crystals and quantum thermalization in closed systems [24–28].

Disorder and interactions are identified as key controlling parameters driving a thermal system towards a MBL phase. In the absence of interactions, a quantum system subjected to arbitrarily weak disorder potential would be Anderson localized [1,29,30] in one dimension. Many-body localization occurs in one-dimensional (1D) interacting systems in the presence of externally applied random disorder fields [10–14,31–36]. A system can exhibit a thermal-MBL phase transition when the magnitude of the disorder strength (h) is greater than a critical value, $h > h_c$. Usually, this transition occurs through a marginally localized intermediate regime, which may depend on the system size, disorder strength, and the interactions [14,35,37].

MBL has been theoretically proposed in the presence of quasiperiodic static potentials described by the Aubry-Andre model in one dimension [15,38–41]. The onset of thermal-MBL phase transition in this model has been found to be at the critical value $h_c = 2$ (in units of the "kinetic" energy) and followed by a broad marginally localized precursor to the MBL regime [35,38,39]. Recent numerical studies of two-leg ladder model provide signatures of the thermal-MBL transition for both random disorder and the Aubry-Andre model under an externally applied critical field strength in the range $8 < h_c < 10$ [41,42].

Disorder free MBL arises in systems that can dynamically generate their own disorder in the absence of externally applied fields. Proposals in 1D lattices include of out-of-equilibrium bosons [43] or spins [44], or families of models with fermions effectively coupled to spins [45,46]. A two-leg ladder compass model, with discrete translational symmetry and imposed topological constraints on the Hilbert space due to conservation laws, identified a prethermal phase with logarithmic growth of the entanglement entropy in time [47]. It has been shown that the presence of a linearly varying potential in spin chains may disentangle the Hilbert space in discrete

---

[*] Contact author: harshadewa@etec.ruh.ac.lk, uchoa@ou.edu

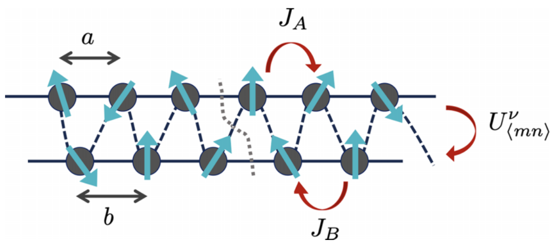

FIG. 1. Schematic of the two isotropic Heisenberg spin chains having lattice parameters a and b. The isotropic spin interaction within each chain is described by J_A and J_B. The short-range NN exchange coupling between chains at direction ν, $U^{\nu}_{\langle nm\rangle}$, is guided by the black dashed line. The dotted curved line represents a bipartite cut employed to calculate the time evolution of the entanglement entropy between left and right parts of the system.

sectors, resulting in nonergordic MBL-like dynamics [21,48–53]. In another proposal, two coupled fermionic chains with full translational symmetry, each chain having a different species with either heavy or light masses, were found to have early time evolution indications of MBL [54–58]. Translationally invariant systems, nevertheless, show strong finite-size effects and are expected to delocalize in the thermodynamic limit at long times [57,58]. Moreover, implementation of some of the other proposals requires the preparation of specifically ordered states in finely tuned Hamiltonians.

In this work we address the question of whether the quasiperiodic coupling between two isotropic spin chains, each one with discrete translational symmetry, can produce a robust MBL phase. We show that the answer is affirmative. We propose a model consisting of two isotropic spin chains coupled to each other by an anisotropic short-range exchange interaction of the XXZ type that decays exponentially with distance. The two spin chains have different incommensurate lattice parameters a and b. The ratio between lattice parameters is irrational,

$$\frac{b-a}{a} \equiv \gamma\delta, \tag{1}$$

where $\delta > 0$ is a real number and γ is some irrational number whose value is chosen to be $\gamma = (1 - \pi^2/10)$, with $0 \leqslant \gamma\delta < 1$. This construction results in two coupled spin chains with incommensurate lattice constants. Because their exchange coupling decays exponentially with the distance between spin sites, the two chains are quasiperiodically coupled to each other, as indicated in Fig. 1.

In the Ising limit of the XXZ exchange between the chains, we show that this system enters a MBL phase above a critical value of the quasiperiodic interchain exchange coupling. Such critical value is strongly dependent on the incommensuration. We provide numerical evidence that the MBL phase is optimized for $0.176 < \gamma\delta < 0.712$ and is suppressed in the commensurate limit $\gamma\delta \to 0$. In the optimal regime, the MBL phase emerges when the interchain exchange coupling in the z spin axis $U_0^z/J > 9$, with J the isotropic intrachain Heisenberg exchange coupling, while a prethermal phase appears between $6 < U_0^z/J < 9$. In the latter, the entanglement entropy grows logarithmically with time. Below $U_0^z/J < 6$ the system is in the thermal phase for most incommensuration values.

We find that restoration of the interchain exchange coupling in the x and y spin directions, U_0^{xy}, significantly enhances entanglement between the chains and produces delocalization. In the isotropic limit $U_0^{xy} = U_0^z$, the system is always in the thermal phase. For strong but finite anisotropy, the MBL phase is stabilized at $U_0^z/J > 30$ for $U_0^{x,y}/J = 1$ near the optimal incommensuration $\gamma\delta \approx 0.391$. In this regime thermalization occurs at $U_0^z/J < 9$, with a broad prethermal region in between.

The structure of the paper is as follows: in Sec. II we describe the Hamiltonian of the system and proceed to calculate the time evolution of the bipartite entanglement entropy S in Sec. III. In the Ising limit of the XXZ interchain exchange, we show that the entanglement entropy follows a transition from volume law to area law scaling at finite incommensuration, as the exchange coupling between the chains is increased. Next, using exact diagonalization at zero magnetization, we calculate the averaged inverse participation ratio (IPR) for finite system sizes as a function of the incommensuration and the exchange coupling. We extrapolate the IPR to the thermodynamic limit and construct the phase diagram separating the thermal and MBL phases. To check for the stability of the MBL phase in the Ising limit of the XXZ exchange between the chains, we restore the interchain exchange interaction along the x and y spin directions. We examine the time evolution of the entanglement entropy to show that the MBL phase remains stable, although at a much larger interchain critical coupling U_0^z. We also calculate the IPR of the ground state for very large system sizes using density matrix renormalization group (DMRG) to gain insight into the behavior of the system in the $\gamma\delta \to 0$ limit. Finally, in Sec. IV we present our conclusions.

II. COUPLED SPIN CHAIN MODEL

We consider two isotropic spin-$\frac{1}{2}$ Heisenberg chains with Hamiltonian

$$\mathcal{H}_\alpha = J_\alpha \sum_{i=1}^{N_\alpha} \mathbf{S}_i \cdot \mathbf{S}_{i+1}, \tag{2}$$

where $\alpha = A, B$ labels each chain, and $J_\alpha > 0$ is the intrachain nearest-neighbor (NN) exchange coupling. N_α is the number of spins on chain α and $\mathbf{S} = (S^x, S^y, S^z)$ is the spin operator $S^\nu = \frac{\hbar}{2}\sigma^\nu$, with $\nu = x, y, z$ labeling the standard Pauli matrices. The spin chains are coupled to each other through the XXZ exchange

$$\mathcal{H}_{AB} = \sum_{\nu=x,y,z} \sum_{n\in A, m\in B} U^\nu_{nm} S^\nu_n S^\nu_m, \tag{3}$$

where $U^x_{nm} = U^y_{nm} \equiv U^{xy}_{nm}$ and U^z_{nm} are the interchain exchange couplings for spins oriented in the x, y, z directions. The interchain exchange decays exponentially with the distance between sites,

$$U^\nu_{nm} = U^\nu_0 \mathrm{e}^{\rho\left(1-\sqrt{1+r^2_{nm}}\right)}, \tag{4}$$

where $r_{nm} = |R^A_n - R^B_m|/d$ is the horizontal distance between sites normalized by the distance between the two chains d, and ρ sets the range of the interaction. R^ν_n is the position of

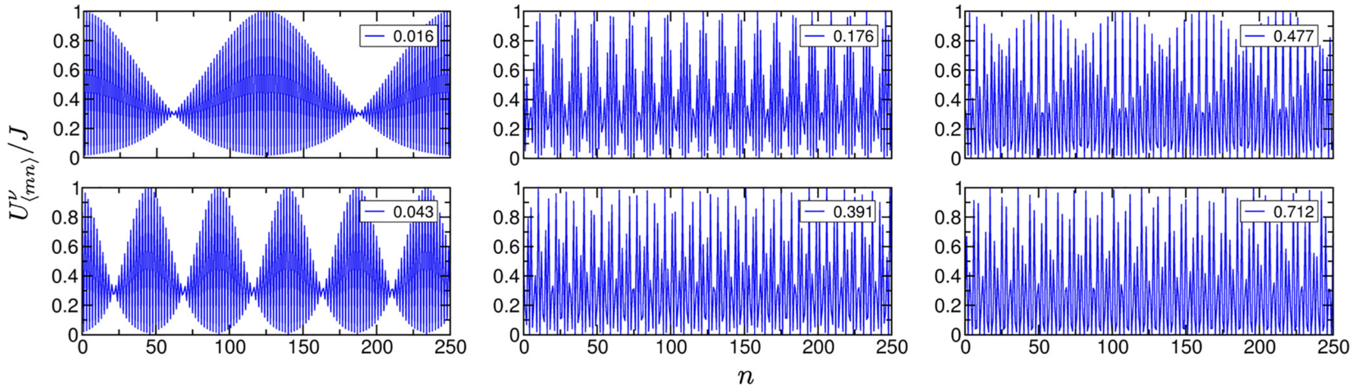

FIG. 2. Evolution of the interchain interaction profile for NN sites, $U^{\nu}_{\langle nm\rangle}/J$ vs the site position n in the spin ladder for different values of incommensuration $\gamma\delta$, with $\gamma = (1 - \pi^2/10)$ an irrational number. n sites below to chain A and m sites to chain B. The legends represent the approximate value of $\gamma\delta$ for each potential profile. $\delta = e^{0.2}, e^{1.2}, e^{2.6}, e^{3.4}, e^{3.6}$, and e^4 for $\gamma\delta \approx 0.016, 0.043, 0.176, 0.391, 0.477$, and 0.712, respectively.

the spins along the chains,

$$R^A_n = an - r^A_0, \qquad R^B_m = bm - r^B_0, \tag{5}$$

with a and b the lattice parameters of spin chains A and B, respectively, and r^{α}_0 is the origin of each chain.

The primary focus of this work is to investigate the effect of interchain exchange coupling in the onset of the MBL transition. We finely tune $J_A = J_B = J$ so that in the limit $U^{\nu}_0 \to 0$ the system decouples into two identical isotropic Heisenberg spin chains, which are ergodic. The exchange coupling between chains $U^{\nu}_{\langle nm\rangle}$ given in Eq. (3) is truncated to the two NN spin sites, as shown in Fig. 1. The solid lines connecting spin sites in each chain represent the isotropic interactions between spins in each chain. The dashed line running between spin sites is a guide to the eye representing the short-range exchange coupling between chains. Thus, each spin in a chain couples through J with two NNs in the same chain and through $U^{\nu}_{\langle nm\rangle}$ with up to two nearest spins in the opposite chain. We set $\rho = 10$ in Eq. (4). Our conclusions do not depend on the choice of ρ, which will at most rescale the localization length at finite system sizes, but not in the thermodynamic limit.

We consider the regime where the incommensuration is in the range $0 \leqslant \gamma\delta < 1$, in which the lattice parameters satisfy $b \in [a, 2a]$. For large incommensurations $\gamma\delta \gg 1$, the linear bond density between chains is reduced, as spin chain B becomes sparse, and the two spin chains effectively decouple. The evolution of the profile of the interchain interaction between NN spins $U^{\nu}_{\langle nm\rangle}$ with the incommensuration is shown in Fig. 2.

III. METHODS AND RESULTS

The many-body quantum states of the total Hamiltonian

$$\mathcal{H} = \mathcal{H}_A + \mathcal{H}_B + \mathcal{H}_{AB} \tag{6}$$

can be described using 2^N basis vectors spanning the Hilbert space, with $N = N_A + N_B$ the total number of sites in the spin ladder. The basis vectors are constructed with product states $|s_1\rangle \otimes \cdots \otimes |s_N\rangle$, where $|s_i\rangle = |\uparrow\rangle, |\downarrow\rangle$ are the eigenstates of S^z_i on site i. By convention, the product states are arranged from left to right in ascending order as guided by the dashed line in Fig. 1. We use the above ordered set of basis vectors to calculate the matrix elements of $\mathcal{H}$ and construct the matrix product state (MPS) in our numerical calculations.

We numerically calculate the time evolution of an initial product state following a global quantum quench using the unitary transformation, $|\psi(t)\rangle = e^{-i\mathcal{H}t}|\psi_0\rangle$. The initial state is chosen so that the spins in each chain are arranged in a Néel state. For instance, at low incommensuration ($\gamma\delta \approx 0$) the initial product state is given by $|\psi_0\rangle = |\uparrow, \uparrow, \downarrow, \downarrow, \ldots, \uparrow, \uparrow\rangle$. We use MPS to represent the quantum many body system and study the dynamics following the time-evolving block decimation (TEBD) method. In TEBD method, the time evolution operator $e^{-iH\tau}$ is decomposed into the product of locally interacting pair of spins using a second-order Trotter decomposition and contracted with the MPS to obtain the updated quantum state after time τ (see the Appendix). This process is repeated t/τ time steps to obtain the quantum state of the system after time t. The maximum time step used is $\tau = 0.05J^{-1}$. The internal bond dimension of the MPS can be truncated in low-entangled systems to improve computational efficiency. In this work, we use a weight cutoff of 10^{-7} in the MPS of the thermal phase. In the MBL phase we used a MPS bond dimension of 50.

A. Entanglement entropy

The spin ladder is bipartitioned with a vertical cut into two spin ladders with $N/2$ of spins, as shown in Fig. 1. We study the development of entanglement between the left and the right half of the system with time. The reduced density matrix of the left half of the system (ρ_L) is calculated by tracing out the quantum degrees of freedom of right half. This quantity is a probabilistic measure of the entanglement developed through $2^{N/2}$ bonds between the left and the right halves of the system. Thus, the von Neumann bipartite entanglement entropy is calculated as $S = -\mathrm{tr}_L[\rho_L \ln(\rho_L)]$.

Volume law versus area law. We investigate the role of the exchange coupling between chains and the amount of incommensuration in the MBL transition. We first turn off the spin flip exchange interaction between two chains by

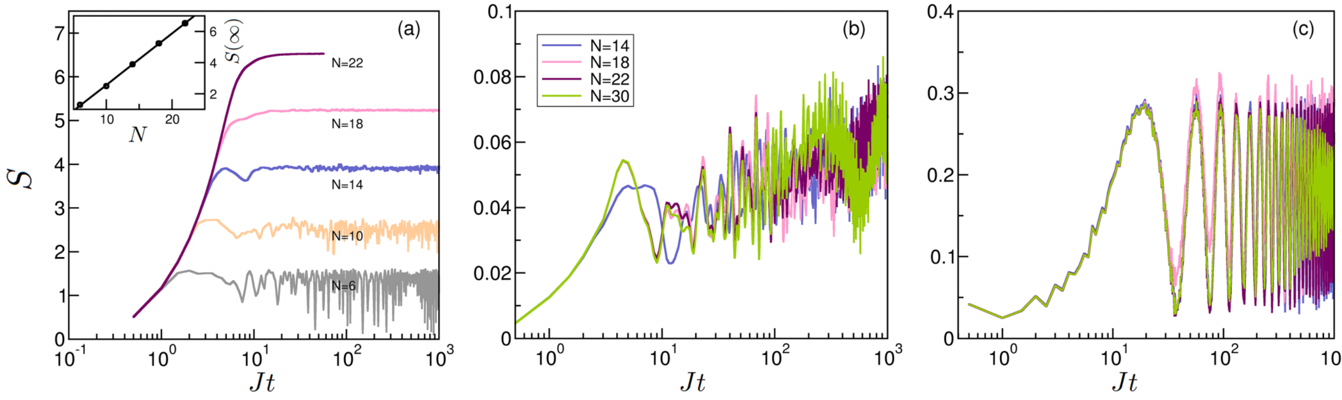

FIG. 3. Time evolution of the bipartite entanglement entropy $S(t)$ following a quantum quench from an initial product state for different system sizes. (a) Thermal phase at $\delta = 1.0$ ($\gamma\delta \sim 0.013$), $U_0^z/J = 1$ and $U_0^{xy} = 0$ for $N = 6, 10, 14, 18$, and 22. The entropy saturates due to the finite-size effects. The saturated entropy follows the volume law of entanglement. Inset: Plot of the saturated entropy $S(\infty)$ vs number of ladder spins N in the thermal phase. The slope of the straight line is 0.3305. MBL phase at $\delta = 15.0$ ($\gamma\delta \sim 0.196$), $U_0^z/J = 25$ and $U_0^{xy} = 0$ for (b) $r_0^A = Na/2 + 0.5$ and $r_0^B = Nb/2 + 0.6$ and (c) $r_0^A = Na/2$ and $r_0^B = Nb/2 + 0.3$. Different curves correspond to different system sizes. The relative placement of the two chains is adjusted to keep bond strength at the bipartite cut independent of the system size. In either case, the curves collapse on top of each other, consistently with area law entanglement (see text).

setting $U_0^{xy} = 0$. Choosing the relative position of the two spin chains to be $r_0^A = r_0^B = 0$, we show in Fig. 3 that the bipartite entanglement entropy S follows a transition from volume law entanglement to area law as a function of U_0^z and $\gamma\delta$. Figure 3(a) shows the time evolution of S for $\delta = 1.0$ ($\gamma\delta \approx 0.013$) and $U_0^z/J = 1$ at different system sizes. As time elapses, S initially grows quickly and eventually saturates close to the maximum possible value of entanglement entropy for half system, $N \ln(2)/2 \approx 0.3466N$. The saturated entropy $S(\infty)$ scales linearly with the size of the system N [see inset of Fig. 3(a)] with a slope of 0.3305. Thus, the system is in the thermal phase and follows a volume law of entanglement. Those results are independent of the choices of r_0^A and r_0^B.

At higher values of U_0^z and incommensuration the system has area law entanglement across the left and right partitions. In Figs. 3(b) and 3(c), we plot the time evolution of S for $\delta = 15.0$ ($\gamma\delta \approx 0.196$) and $U_0^z/J = 25$ in four different system sizes: $N = 14$, 18, 22, and 30. We adjust the relative placement of the chains through r_0^A and r_0^B to ensure that the bond strength $U^z_{\langle\bar{n}\bar{m}\rangle}$ at the bipartite cut ($\bar{n} = N/2$) is independent of the chain size. Figure 3(b) depicts the evolution of the $S(t)$ curves for $r_0^A = Na/2 + 0.5$ and $r_0^B = Nb/2 + 0.6$, where the bond strength at the partition is $U^z_{\langle\bar{n}\bar{m}\rangle} = 0.46$ for all N. Figure 3(c) depicts the behavior of $S(t)$ for a different choice of relative placement of the chains, $r_0^A = Na/2$ and $r_0^B = Nb/2 + 0.3$, where the bond strength at the bipartite cut is $U^z_{\langle\bar{n},\bar{m}\rangle} = 1.2$. In both cases, $S(t)$ is independent of N. The different curves for several chain sizes collapse into a single curve. The system has thus area law entanglement and is many-body localized up to the longest timescales $t \sim 10^3 J^{-1}$ observed in our simulations.

B. MBL phase diagram

To quantify the MBL transition over a broader range of parameters and extract the thermal-MBL phase diagram, we calculate the mean inverse participation ratio (IPR) of the full energy spectrum at infinite temperature using exact diagonalization. We impose that the system has zero net magnetization and restrict the size of the Hilbert space by picking only the $N!/(N/2)!)^2$ basis vectors that have the same total number of $|\uparrow\rangle$ and $|\downarrow\rangle$ states. The Hamiltonian matrix of Eq. (6) is diagonalized to obtain the full eigenspectrum of the system. The IPR is calculated through the average

$$\langle I\rangle = \frac{1}{D}\sum_{\lambda=1}^{D}\frac{4}{N}\sum_{i}^{N}\langle\phi_\lambda|S_i^z|\phi_\lambda\rangle^2, \tag{7}$$

where $|\phi_\lambda\rangle$ is the λth eigenvector and D is the number of eigenvectors in the system. For a maximally localized (thermalized) phase, $\langle\phi_\lambda|S_i^z|\phi_\lambda\rangle = \pm\frac{1}{2}$ (0) at each spin site, and hence $\langle I\rangle$ takes the value 1 (0). We calculate the IPR for each value of U_0^z/J and incommensuration $\gamma\delta$ in five system sizes, $N = 8, 10, 12, 14, 16$, and then extrapolate to the thermodynamic limit ($N \to \infty$), $\langle I\rangle_\infty$. Following the procedure described in Ref. [35], we adopt the ansatz

$$\frac{\langle I\rangle}{1-\langle I\rangle} \propto N^{\alpha}, \tag{8}$$

from which we extract the scaling exponent α. In ideally thermalized states, where the system is entirely delocalized and ergodic, $\alpha < -1$ with $\langle I\rangle_\infty \sim 0$. On the other hand, in the MBL phase, one expects $\alpha > 0$ with $\langle I\rangle_\infty \sim 1$.

Phase diagram. The thermal-MBL phase diagram is drawn in the left panel of Fig. 4, where we plot $\langle I\rangle_\infty$ against the interchain coupling U_0^z and the incommensuration $\gamma\delta$. The black solid line, drawn at $\langle I\rangle_\infty = 0.1$, separates the thermal phase (dark red) from the marginally localized and MBL phases (light red and bright yellow, respectively). The system is in the thermal phase for all values of U_0^z/J below the the critical exchange coupling at the phase separation line (solid black). This phase separation approximately corresponds to the boundary of the region in the right panel of Fig. 4 where the scaling exponent $\alpha < -1$. The system is in the thermal phase when $U_0^z/J \lesssim 6$ for all values of $\gamma\delta < 0.8$.

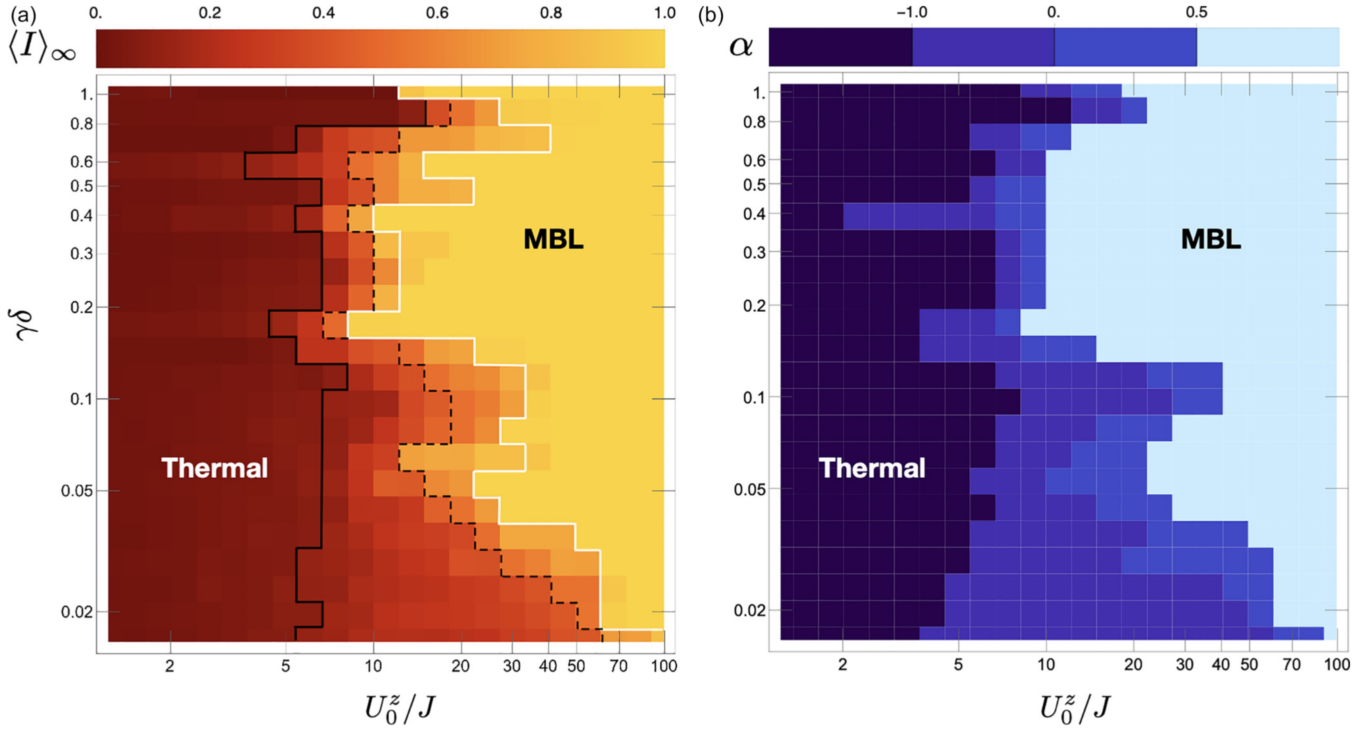

FIG. 4. Numerical phase diagram between thermal and MBL phases. (a) Color plot of the mean inverse participation ratio extrapolated to the thermodynamic limit $\langle I\rangle_\infty$ vs incommensuration $\gamma\delta$ and strength of exchange coupling between the chains U_0^z/J. (b) Color plot of the exponent α extracted in the extrapolation of $\langle I\rangle$ to the thermodynamic limit versus $\gamma\delta$ and U_0^z/J. The onset of the thermal-MBL phase separation (black solid line) is drawn at $\langle I\rangle_\infty = 0.1$. The thermal region (dark red) to the left of the line corresponds approximately to the region where scaling exponent $\alpha < -1.0$ in panel (b). The black dashed line is drawn at $\langle I\rangle_\infty = 0.5$. The solid white line is at $\langle I\rangle_\infty = 0.9$, and the region to its right in bright yellow is in the MBL phase. This region approximately matches the light blue region in panel (b), where $\alpha > 0.5$. The intermediate region between the solid black and solid white lines is marginally localized ($0.1 < \langle I\rangle_\infty < 0.9$). This region corresponds to the range of scaling exponents $-1 < \alpha < 0.5$ in panel (b).

The region where U_0^z/J is larger than the critical value set by the solid white line is identified as fully many-body localized (yellow region), where $\langle I\rangle_\infty > 0.9$. It correlates with the region shown in light blue in the right panel, where $\alpha > 0.5$. The black dashed line is drawn at $\langle I\rangle_\infty = 0.5$ and approximates the boundary where $\alpha = 0$ in the right panel. It is clear that the onset of the MBL phase has a strong dependence on the incommensuration. In the analysis of both $\langle I\rangle_\infty$ and the scaling exponent α, the optimal incommensuration for the onset of MBL is in the range $0.176 < \gamma\delta < 0.712$, where the critical exchange coupling is $U_0^z/J \sim 10$. At low incommensurations, $\gamma\delta \lesssim 0.1$, the MBL phase is strongly suppressed. In particular, in the limit $\gamma\delta \to 0$, where the coupling between the spin chains becomes periodic, we observe no MBL. In the opposite limit, $\gamma\delta \to 1$, the bond density between the chains decreases as the lattice constant of one chain becomes nearly twice as the constant of the other chain. In this regime the critical coupling needed for MBL increases.

The light red region in the left panel of Fig. 4 corresponds to an intermediate phase with $0.1 < \langle I\rangle_\infty < 0.5$ where the states are marginally localized. The entanglement entropy in this prethermal phase scales logarithmically with time, in contrast with the scaling in the MBL and thermal phases shown in Fig. 3. This region approximately matches the midregion in the right panel, where $-1 < \alpha < 0$. The width of this region is very broad at low incommensuration, reflecting the suppression of MBL, but narrows down at $\gamma\delta \geqslant 0.176$. This appears to be due to the development of rapid oscillations in the profile of the exchange interaction between the chains $U^z_{\langle nm\rangle}$ at $\gamma\delta \approx 0.176$, as shown in Fig. 2. The boundaries separating the prethermal phase from the thermal and MBL phases are consistent in both panels, although not smooth. The roughness indicates the presence of numerical errors induced by the extrapolation to the thermodynamic limit. We estimate the error bar in the inverse participation ratio $\langle I\rangle_\infty$ and in the scaling exponent α to be around 10%.

The extrapolation of $\langle I\rangle$ to the thermodynamic limit in small system sizes is meaningful for interaction potentials that oscillate rapidly compared to the system size. The extrapolated results appear to be fairly accurate in the region $\gamma\delta > 0.2$. The extrapolation becomes less accurate in the opposite regime, at low incommensuration. In any case, we note that this procedure correctly captures the expected suppression of MBL in the low incommensuration limit $\gamma\delta \to 0$.

C. Delocalization due to spin flips between chains

We now turn on the exchange interaction between the spin chains U_0^{xy}, which produces spin flips. Spin flips between chains map through the standard Jordan-Wigner transformation into interchain hopping in the fermionic language, which could lead to delocalization. We numerically observe that this term drastically lowers $\langle I\rangle$ in the finite-size systems we simulated ($N \leqslant 18$). Observation of MBL through IPR

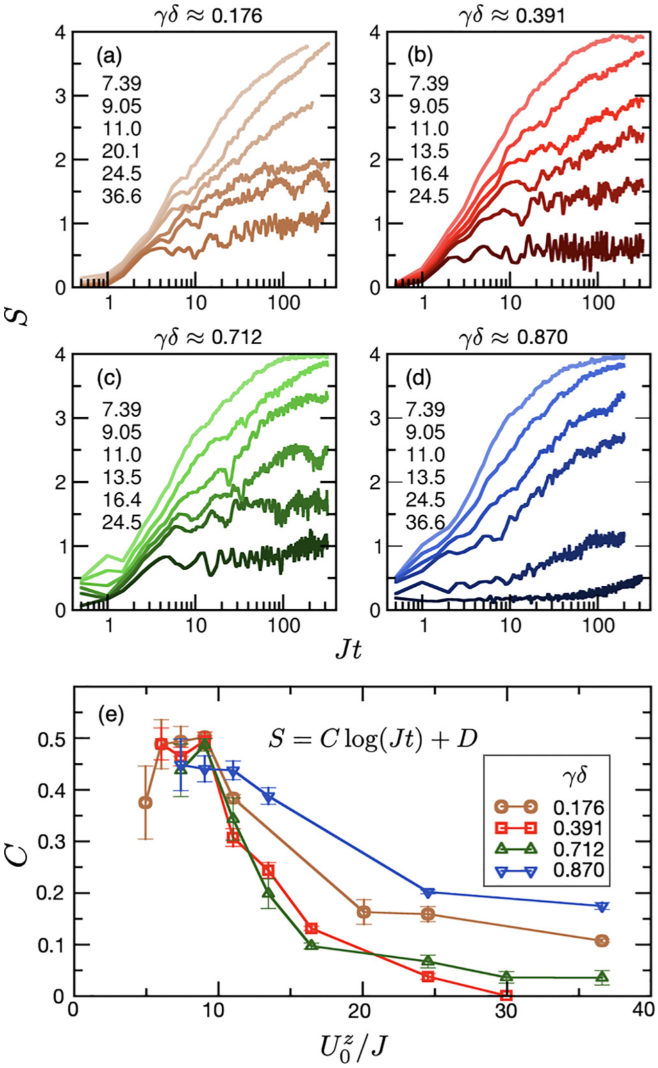

FIG. 5. Time evolution of the bipartite entanglement entropy S at $U_0^{xy}/J = 1$ for different incommensurations: (a) $\gamma\delta \approx 0.176$, (b) $\gamma\delta \approx 0.391$, (c) $\gamma\delta \approx 0.712$, and (d) $\gamma\delta \approx 0.870$. Top to bottom curves in each panel correspond to ascending values of U_0^z/J indicated on the left of the curves. (e) Slope of the entanglement entropy C extracted from the logarithmic fit of the curves in panels (a) to (d). The system enters in the MBL phase when $C = 0$.

over the whole energy spectrum would hence require much larger system sizes in order to properly extrapolate the data to the thermodynamic limit. This can be challenging given the exponential growth in computational cost in exact diagonalization methods. To gain insight, we resort to calculate the time evolution of the entanglement entropy $S(t)$ through MPS. Even though MPS is relatively efficient, interchain spin flip processes considerably increase the entanglement of the states, requiring a much larger bond dimension for the MPS compared to the $U_0^{xy} = 0$ case.

In Figs. 5(a)–5(d) we show the time evolution of the bipartite entanglement entropy calculated from the initial state $|\uparrow, \downarrow, \uparrow, \downarrow, \dots\rangle$ for $U_0^{xy}/J = 1$ at four different incommensurations, $\delta = e^{2.6}$ for $N = 18$ and $e^{3.4}, e^{4.0}$, and $e^{4.2}$ for $N = 14$ ($\gamma\delta \approx 0.176, 0.391, 0.712$, and 0.870, respectively). Each panel shows six curves ordered from top to bottom with increasing values of U_0^z/J ranging from 7 to 36. We observe logarithmic growth of S at long times before reaching the saturation, a characteristic signature of a precursor to the MBL phase in the parameter space. At sufficiently long times, this phase is expected to thermalize.

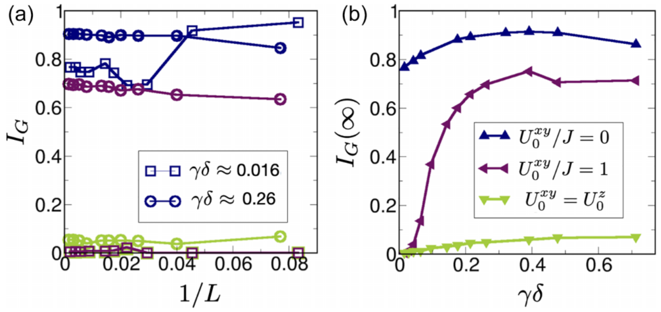

FIG. 6. DMRG calculation of the ground state inverse participation ratio I_G for $U_0^z/J = 7.39$ and $U_0^{xy}/J = 0$ (blue curves), $U_0^{xy}/J = 1$ (purple), and $U_0^{xy} = U_0^z$ (green). (Left) I_G vs inverse of the system size $1/L$ for $\gamma\delta \approx 0.016$ (squares) and $\gamma\delta \approx 0.26$ (circles). (Right) Thermodynamic limit of the ground state inverse participation ratio $I_G(\infty)$ for $L \to \infty$ vs incommensuration $\gamma\delta$.

In order to characterize the MBL transition, we fit the curves with the form $S(t) = C\log(Jt) + D$ and extract the slope C. In Fig. 5(e) we plot the slope of the curves as a function of U_0^z. We average over two different initial product states, $|\uparrow, \downarrow, \uparrow, \downarrow, \dots\rangle$ and $|\uparrow, \uparrow, \downarrow, \downarrow, \dots\rangle$, and different initial times. The values of C for different system sizes are scaled to $N = 14$. The behavior of C with U_0^z shows a broad peak followed by a monotonic decrease with increasing U_0^z starting at $U_0^z/J = 9.2$ for all incommensurations inside the previously identified optimal range $0.176 < \gamma\delta < 0.712$. The broad peak corresponds to a thermal phase that saturates early due to finite size effects. The point at which the slope starts to decrease monotonically with increasing U_0^z can be identified as the onset of the thermal-MBL transition, with marginally localized states. The rate of decrease of the slope C varies with the incommensuration. The system enters in the MBL phase only when $C \to 0$. We note that this is the case at $\gamma\delta \approx 0.391$ for $U_0^z/J \approx 30$ where $C = 0.001$. The slope nevertheless decreases much slower for other incommensuration values, indicating the broadening in size of the marginally localized region as the boundary to the MBL phase retreats. This picture is qualitatively consistent with an overall shift of the MBL phase separation line (white) to the right in Fig. 4, combined with the emergence of a narrower range of optimal incommensuration for the MBL phase that is centered around $\gamma\delta \approx 0.391$. To develop more insight on the effect of delocalization in the limit of $\gamma\delta \to 0$, we use DMRG to calculate the inverse participation ratio of the ground state I_G [59]. This quantity is calculated for system sizes ranging from $N = 24$ to 1100, with $L \sim \frac{N}{2}$. DMRG results are useful predictors for thermal phases. Even though the presence of localization in the ground state does not inform about the behavior of the system at infinite temperature, where it can delocalize, delocalization in the ground state can conclusively rule out the emergence of MBL in the thermodynamic limit.

Figure 6(a) shows the variation of I_G with the inverse of the size of the chains $1/L$ at $U_0^z/J = 7.39$ for $U_0^{xy}/J = 0$, 1 and

$U_0^{xy} = U_0^z$ (blue, purple, and green curves, respectively). The thermodynamic limit of I_G at $L \to \infty$ [$I_G(\infty)$] for $U_0^{xy}/J = 0$ (blue curves) indicates localization of the ground state irrespective of the incommensuration ($\gamma\delta \approx 0.016$ and 0.26). This behavior is consistent with the fact that the ground state of the isotropic antiferromagnetic Heisenberg model for a single spin chain has gapped spinon excitations [60,61]. Those gapped excitations remain stable in the presence of an Ising exchange coupling with another chain ($U_0^{xy} = 0$) in the $\gamma\delta \to 0$ limit. This is confirmed in Fig. 6(b), where we plot $I_G(\infty)$ as a function of the incommensuration $\gamma\delta$. The blue curve shows that $I_G(\infty) \approx 0.79$ at $\gamma\delta \approx 0$. For the chosen set of couplings, the phase diagram in Fig. 4 reveals that the system will eventually delocalize in the infinite temperature regime through a prethermal phase.

For finite anisotropy in the XXZ exchange between the chains, we observe a significant reduction of $I_G(0)$ with increasing U_0^{xy}/J. For $U_0^z/J = 7.39$ and $U_0^{xy}/J = 1$ (purple solid line) $I_G(\infty)$ peaks at $\gamma\delta \approx 0.391$, where it has a kink. This is qualitatively consistent with MPS results for the time evolution of the entanglement entropy shown in Fig. 5, which optimizes MBL at the same incommensuration. At smaller values of $\gamma\delta$, $I_G(\infty)$ decreases rapidly and goes to zero in the $\gamma\delta \to 0$ limit. This suggests that the whole energy spectrum is delocalized in the commensurate limit. In the isotropic limit of the XXZ exchange between the chains, $U_0^{xy} = U_0^z$, $I_G(\infty) \ll 1$ for all incommensurations (green curves in Fig. 6), consistent with a thermal phase.

IV. CONCLUSION

We showed that robust MBL emerges from two quasiperiodically coupled Heisenberg spin chains. Using a combination of different numerical methods, we derived the thermal-MBL phase diagram of this problem as a function of the interchain exchange coupling and the incommensuration. We show that the MBL phase is optimal in the Ising limit of the XXZ interchain exchange interaction, over a whole range of incommensurations $0.176 < \gamma\delta < 0.712$. Spin flip processes between chains produce a significant amount of entanglement and favor a prethermal phase. MBL is generically present at finite incommensuration above a critical exchange coupling U_0^z in the anisotropic regime $U_0^{xy}/U_0^z \ll 1$, and is entirely suppressed in the isotropic limit of the XXZ exchange interaction. This proposal does not require finely tuned Hamiltonians and could be implemented in spin chains constructed in the absence of externally applied potentials.

ACKNOWLEDGMENTS

We thank J. Knolle and A. Auerbach for insightful discussions. B.U. was supported by NSF (US) DMR-2024864. K.G.S.H.G. acknowledges UOR for support.

APPENDIX: NUMERICAL CALCULATION OF THE TIME EVOLUTION OF STATE $|\psi\rangle$

In this Appendix, we provide numerical details of the time evolving block decimation (TEBD) method adopted to describe the time evolution of states according to Hamiltonian (6). We provide a comparison of the numerical results of the bipartite entanglement entropy $S(t)$ against exact diagonalization.

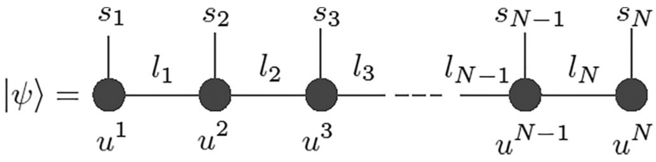

FIG. 7. Diagrammatic notation of the Matrix Product State (MPS) tensor train.

A many-body quantum state can be described by the linear superposition of 2^N basis vectors

$$|\psi\rangle = \sum_{s_i} c_{s_1 s_2 \ldots s_N} |s_1 s_2 \ldots s_N\rangle, \tag{A1}$$

where $|s_i\rangle$ are the eigenstates of S_i^z with $|\uparrow\rangle$ or $|\downarrow\rangle$ spin states. The quantum state (A1) can be represented in the form of a matrix product state (MPS) as

$$|\psi\rangle = \sum_{s_i} u^1_{s_1 l_1} u^2_{l_1 s_2 l_2} u^3_{l_2 s_3 l_3} \ldots u^{N-1}_{l_{N-1} s_{N-1} l_N} u^N_{l_N s_N} \times |s_1 s_2 \ldots s_N\rangle, \tag{A2}$$

where u^p_{ijl} are tensors of rank 3 at spin site p. These are associated with the basis vectors generated by the tensor product $|s_1\rangle \otimes \cdots \otimes |s_N\rangle$ and can be represented by the diagrammatic notation shown in Fig. 7.

The time evolution of a quantum state $|\psi\rangle$ is described by the unitary operator, $U(\tau) = e^{-i\mathcal{H}\tau}$, where $\mathcal{H}$ is the time-independent Hamiltonian. The state at time $\tau + t_0$, $|\psi(\tau + t_0)\rangle$ can be given by applying the time evolution operator $U(\tau)$ to the initial state $|\psi(t_0)\rangle$

$$|\psi(\tau + t_0)\rangle = e^{-i\mathcal{H}\tau} |\psi(t_0)\rangle. \tag{A3}$$

Hamiltonian (6) can be written as the sum of locally interacting pairs of spins. We decompose the Hamiltonian into two parts: interactions within isotropic chains $\mathcal{H}_0 = \mathcal{H}_A + \mathcal{H}_B \equiv \sum_{i,j} h_{ij}$, where the pairs i, j are interacting NN spins in the same chain, and interchain interactions $\mathcal{H}_{AB} \equiv \sum_{n,m} g_{nm}$, with the pairs n, m denoting interacting NN spins in opposite chains. The locally interacting pairs of spins h_{ij} and g_{mn} are called gates. The basis states are arranged in ascending order as shown in Fig. 1. Thus, at low values of incommensuration ($\gamma\delta \ll 1$), $j = i + 2$ and $m = n + 1$.

The time evolution operator can be written as

$$U(\tau) = e^{-i(\mathcal{H}_0 + \mathcal{H}_{AB})\tau}. \tag{A4}$$

We now write Eq. (A4) as a product of gates h_{ij} and g_{nm}, so that the operator $U(\tau)$ can be contracted with the MPS in Eq. (A2) to numerically evaluate $|\psi(\tau + t_0)\rangle$. Since $[\mathcal{H}_0, \mathcal{H}_{AB}] \neq 0$, we adopt a second-order Trotter decomposition

$$e^{-i(\mathcal{H}_0 + \mathcal{H}_{AB})\tau} \approx e^{-i\mathcal{H}_{AB}\tau/2} e^{-i\mathcal{H}_0\tau/2} e^{-i\mathcal{H}_0\tau/2} e^{-i\mathcal{H}_{AB}\tau/2} + O(\tau^3). \tag{A5}$$

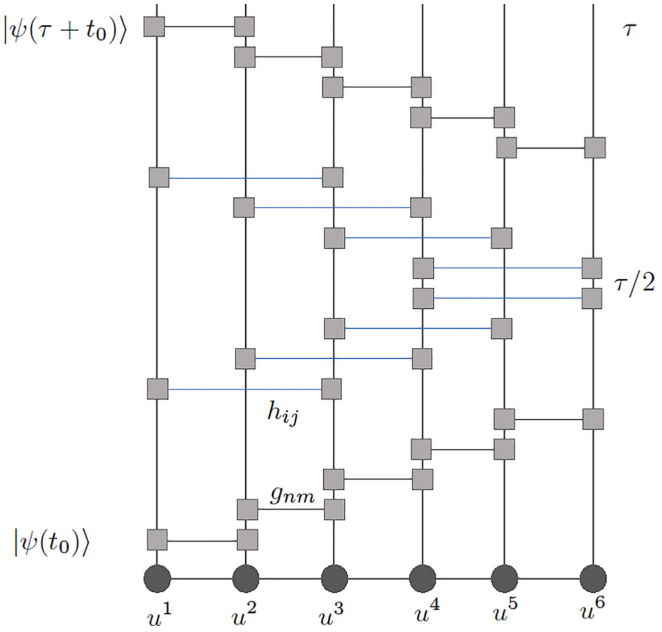

FIG. 8. Diagrammatic notation of the time evolution algorithm (for time step τ) following the second-order Trotter decomposition. The algorithm is shown only for a system of $N = 6$. The two rectangles connected by a thin horizontal line represent the operators h_{ij} and g_{nm}. The solid circles represent the MPS at initial time t_0, $|\psi(t_0)\rangle$.

Similarly, we can expand the decomposition to individual gates. Equation (A3) can be implemented numerically as shown in the diagrammatic notation in Fig. 8.

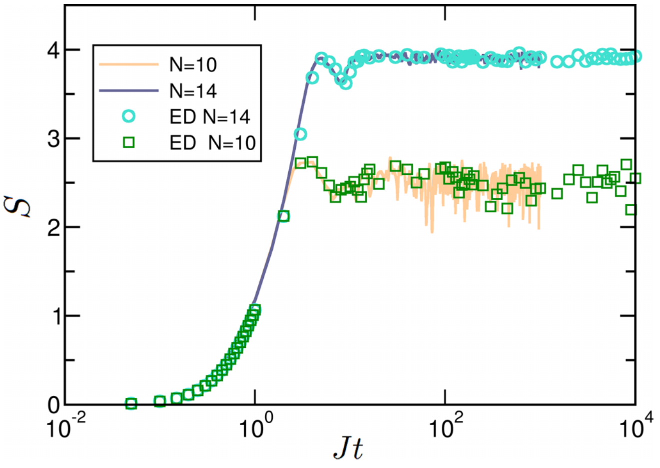

FIG. 9. Plot of time evolution of the entanglement entropy of the system shown in Fig. 1 for $\gamma\delta = 0.013$, $U_0^z/J = 1$, and $U_0^{xy}/J = 0$. The solid lines represent the results of numerical calculation using the algorithm shown in Fig. 8. The time step used is $\tau = 0.05J^{-1}$. A weight cutoff 10^{-7} is employed in *Julia* code truncating the MPS. The open symbols represent the results from exact diagonalization (ED) for $N = 10$ and $N = 14$.

We calculate the time evolution of the bipartite entanglement entropy with the numerical time evolution of the quantum state calculated using the algorithm represented in Fig. 8. We compare the time evolution of the entanglement entropy (S) calculated using the above numerical time integration procedure with the results from exact diagonalization (ED) in Fig. 9 for $N = 10$ and $N = 14$. The two methods agree and give the same numerical results.

---

[1] P. W. Anderson, Absence of diffusion in certain random lattices, Phys. Rev. **109**, 1492 (1958).
[2] R. Nandkishore and D. A. Huse, Many-body localization and thermalization in quantum statistical mechanics, Annu. Rev. Condens. Matter Phys. **6**, 15 (2015).
[3] M. Rigol, Breakdown of thermalization in finite one-dimensional systems, Phys. Rev. Lett. **103**, 100403 (2009).
[4] D. A. Abanin and Z. Papic, Recent progress in many-body localization, Ann. Phys. **529**, 1700169 (2017).
[5] D. A. Abanin, E. Altman, I. Bloch, and M. Serbyn, Many-body localization, thermalization, and entanglement, Rev. Mod. Phys. **91**, 021001 (2019).
[6] J. Z. Imbrie, Diagonalization and many-body localization for a disordered quantum spin chain, Phys. Rev. Lett. **117**, 027201 (2016).
[7] D. A. Huse, R. Nandkishore, and V. Oganesyan, Phenomenology of fully many-body-localized systems, Phys. Rev. B **90**, 174202 (2014).
[8] E. Altman and R. Vosk, Universal dynamics and renormalization in many-body-localized systems, Annu. Rev. Condens. Matter Phys. **6**, 383 (2015).
[9] D. A. Huse, R. Nandkishore, V. Oganesyan, A. Pal, and S. L. Sondhi, Localization-protected quantum order, Phys. Rev. B **88**, 014206 (2013).
[10] D. Basko, I. L. Aleiner, and B. Altshuler, Metal– insulator transition in a weakly interacting many-electron system with localized single-particle states, Ann. Phys. **321**, 1126 (2006).
[11] J. H. Bardarson, F. Pollmann, and J. E. Moore, Unbounded growth of entanglement in models of many-body localization, Phys. Rev. Lett. **109**, 017202 (2012).
[12] R. Singh, J. H. Bardarson, and F. Pollmann, Signatures of the many-body localization transition in the dynamics of entanglement and bipartite fluctuations, New J. Phys. **18**, 023046 (2016).
[13] M. Serbyn, Z. Papić, and D. A. Abanin, Universal slow growth of entanglement in interacting strongly disordered systems, Phys. Rev. Lett. **110**, 260601 (2013).
[14] D. J. Luitz, N. Laflorencie, and F. Alet, Many-body localization edge in the random-field Heisenberg chain, Phys. Rev. B **91**, 081103(R) (2015).
[15] M. Schreiber, S. S. Hodgman, P. Bordia, H. P. Lüschen, M. H. Fischer, R. Vosk, E. Altman, U. Schneider, and I. Bloch, Observation of many-body localization of interacting fermions in a quasirandom optical lattice, Science **349**, 842 (2015).
[16] A. Lukin, M. Rispoli, R. Schittko, M. Eric Tai, A. M. Kaufman, S. Choi, V. Khemani, J. Léonard, and M. Greiner, Probing entanglement in a many-body– localized system, Science **364**, 256 (2019).

[17] R. Islam, R. Ma, P. M. Preiss, M. Eric Tai, A. Lukin, M. Rispoli and M. Greiner, Measuring entanglement entropy in a quantum many-body system, Nature (London) **528**, 77 (2015).

[18] A. A. Houck, H. E. Türeci, and J. Koch, On-chip quantum simulation with superconducting circuits, Nat. Phys. **8**, 292 (2012).

[19] P. Roushan, C. Neill, J. Tangpanitanon, V. M. Bastidas, A. Megrant, R. Barends, Y. Chen, Z. Chen, B. Chiaro, A. Dunsworth *et al.*, Spectroscopic signatures of localization with interacting photons in superconducting qubits, Science **358**, 1175 (2017).

[20] R. E. Throckmorton and S. Das Sarma, Studying many-body localization in exchange-coupled electron spin qubits using spin-spin correlations, Phys. Rev. B **103**, 165431 (2021).

[21] Q. Guo, C. Cheng, H. Li, S. Xu, P. Zhang, Z. Wang, C. Song, W. Liu, W. Ren, H. Dong *et al.*, Stark many-body localization on a superconducting quantum processor, Phys. Rev. Lett. **127**, 240502 (2021).

[22] P. Zhang, H. Dong, Y. Gao, L. Zhao, J. Hao, J.-Y. Desaules, Q. Guo, J. Chen, J. Deng, B. Liu *et al.*, Many-body Hilbert space scarring on a superconducting processor, Nat. Phys. **19**, 120 (2023).

[23] H. J. Shan, C. M. Dai, H. Z. Shen, and X. X. Yi, Controlled state transfer in a Heisenberg spin chain by periodic drives, Sci. Rep. **8**, 13565 (2018).

[24] J. M. Deutsch, Quantum statistical mechanics in a closed system, Phys. Rev. A **43**, 2046 (1991).

[25] M. Srednicki, Chaos and quantum thermalization, Phys. Rev. E **50**, 888 (1994).

[26] M. Rigol, V. Dunjko, and M. Olshanii, Thermalization and its mechanism for generic isolated quantum systems, Nature (London) **452**, 854 (2008).

[27] L. D' Alessio, Y. Kafri, A. Polkovnikov, and M. Rigol, From quantum chaos and eigenstate thermalization to statistical mechanics and thermodynamics, Adv. Phys. **65**, 239 (2016).

[28] T. Devakul and R. R. P. Singh, Early breakdown of area-law entanglement at the many-body delocalization transition, Phys. Rev. Lett. **115**, 187201 (2015).

[29] J. Billy, V. Josse, Z. Zuo, A. Bernard, B. Hambrecht, P. Lugan, D. Clément, L. Sanchez-Palencia, P. Bouyer, and A. Aspect, Direct observation of Anderson localization of matter waves in a controlled disorder, Nature (London) **453**, 891 (2008).

[30] A. Yamilov, S. E. Skipetrov, T. W. Hughes, M. Minkov, Z. Yu, and H. Cao, Anderson localization of electromagnetic waves in three dimensions, Nat. Phys. **19**, 1308 (2023).

[31] V. Oganesyan and D. A. Huse, Localization of interacting fermions at high temperature, Phys. Rev. B **75**, 155111 (2007).

[32] A. Pal and D. A. Huse, Many-body localization phase transition, Phys. Rev. B **82**, 174411 (2010).

[33] J. A. Kjäll, J. H. Bardarson, and F. Pollmann, Many- body localization in a disordered quantum Ising chain, Phys. Rev. Lett. **113**, 107204 (2014).

[34] A. Chandran, I. H. Kim, G. Vidal, and D. A. Abanin, Constructing local integrals of motion in the many-body localized phase, Phys. Rev. B **91**, 085425 (2015).

[35] D. Vu, K. Huang, X. Li, and S. Das Sarma, Fermionic many-body localization for random and quasiperiodic systems in the presence of short- and long-range interactions, Phys. Rev. Lett. **128**, 146601 (2022).

[36] M. Žnidarič, T. C. V. Prosen, and P. Prelovsek, Many-body localization in the Heisenberg *XXZ* magnet in a random field, Phys. Rev. B **77**, 064426 (2008).

[37] A. Morningstar, L. Colmenarez, V. Khemani, D. J. Luitz, and D. A. Huse, Avalanches and many-body resonances in many-body localized systems, Phys. Rev. B **105**, 174205 (2022).

[38] D. J. Thouless and Q. Niu, Wavefunction scaling in a quasi-periodic potential, J. Phys. A: Math. Gen. **16**, 1911 (1983).

[39] S. Iyer, V. Oganesyan, G. Refael, and D. A. Huse, Many-body localization in a quasiperiodic system, Phys. Rev. B **87**, 134202 (2013).

[40] J. Vidal, D. Mouhanna, and T. Giamarchi, Correlated fermions in a one-dimensional quasiperiodic potential, Phys. Rev. Lett. **83**, 3908 (1999).

[41] J. Hauschild, F. Heidrich-Meisner, and F. Pollmann, Domain-wall melting as a probe of many-body localization, Phys. Rev. B **94**, 161109(R) (2016).

[42] E. Baygan, S. P. Lim, and D. N. Sheng, Many-body localization and mobility edge in a disordered spin-$\frac{1}{2}$ Heisenberg ladder, Phys. Rev. B **92**, 195153 (2015).

[43] G. Carleo, F. Becca, M. Schiró, and M. Fabrizio, Localization and glassy dynamics of many-body quantum systems, Sci. Rep. **2**, 243 (2012).

[44] J. M. Hickey, S. Genway, and J. P. Garrahan, Signatures of many-body localisation in a system without disorder and the relation to a glass transition, J. Stat. Mech.: Theory Exp. (2016) 054047.

[45] A. Smith, J. Knolle, D. L. Kovrizhin, and R. Moessner, Disorder-free localization, Phys. Rev. Lett. **118**, 266601 (2017).

[46] A. Smith, J. Knolle, R. Moessner, and D. L. Kovrizhin, Absence of ergodicity without quenched disorder: From quantum disentangled liquids to many-body localization, Phys. Rev. Lett. **119**, 176601 (2017).

[47] O. Hart, S. Gopalakrishnan, and C. Castelnovo, Logarithmic entanglement growth from disorder-free localization in the two-leg compass ladder, Phys. Rev. Lett. **126**, 227202 (2021).

[48] E. van Nieuwenburg, Y. Baum, and G. Refael, From Bloch oscillations to many-body localization in clean interacting systems, Proc. Natl. Acad. Sci. USA **116**, 9269 (2019).

[49] M. Schulz, C. A. Hooley, R. Moessner, and F. Pollmann, Stark many-body localization, Phys. Rev. Lett. **122**, 040606 (2019).

[50] L.-N. Wu and A. Eckardt, Bath-induced decay of Stark many-body localization, Phys. Rev. Lett. **123**, 030602 (2019).

[51] S. R. Taylor, M. Schulz, F. Pollmann, and R. Moessner, Experimental probes of Stark many-body localization, Phys. Rev. B **102**, 054206 (2020).

[52] R. Yao and J. Zakrzewski, Many-body localization of bosons in an optical lattice: Dynamics in disorder-free potentials, Phys. Rev. B **102**, 104203 (2020).

[53] E. V. H. Doggen, I. V. Gornyi, and D. G. Polyakov, Many-body localization in a tilted potential in two dimensions, Phys. Rev. B **105**, 134204 (2022).

[54] M. Schiulaz and M. Müller, Ideal quantum glass transitions: Many-body localization without quenched disorder, AIP Conf. Proc. **1610**, 11 (2014).

[55] T. Grover and M. P. A. Fisher, Quantum disentangled liquids, J. Stat. Mech.: Theory Exp. (2014) P10010.

[56] M. Schiulaz, A. Silva, and M. Müller, Dynamics in many-body localized quantum systems without disorder, Phys. Rev. B **91**, 184202 (2015).

[57] Z. Papic, E. M. Stoudenmire, and D. A. Abanin, Many-body localization in disorder-free systems: The importance of finite-size constraints, Ann. Phys. **362**, 714 (2015).

[58] N. Y. Yao, C. R. Laumann, J. I. Cirac, M. D. Lukin, and J. E. Moore, Quasi-many-body localization in translation-invariant systems, Phys. Rev. Lett. **117**, 240601 (2016).

[59] U. Schollwöck, The density-matrix renormalization group, Rev. Mod. Phys. **77**, 259 (2005).

[60] P. W. Anderson, The resonating valance bond state in La_2CuO_4 and superconductivity, Science **235**, 1196 (1987).

[61] L. D. Faddeev and L. A. Takhtajan, What is the spin of a spin wave? Phys. Lett. A **85**, 375 (1981).